

## Supplementary Materials for

### **A potentiometric mechanotransduction mechanism for novel electronic skins**

Xiaodong Wu, Maruf Ahmed, Yasser Khan, Margaret E. Payne, Juan Zhu, Canhui Lu\*, James W. Evans, Ana C. Arias\*

\*Corresponding author. Email: [acarias@eecs.berkeley.edu](mailto:acarias@eecs.berkeley.edu) (A.C.A.); [canhuilu@scu.edu.cn](mailto:canhuilu@scu.edu.cn) (C.L.)

Published 24 July 2020, *Sci. Adv.* **6**, eaba1062 (2020)

DOI: [10.1126/sciadv.aba1062](https://doi.org/10.1126/sciadv.aba1062)

#### **The PDF file includes:**

Table S1  
Figs. S1 to S14  
References

#### **Other Supplementary Material for this manuscript includes the following:**

(available at [advances.sciencemag.org/cgi/content/full/6/30/eaba1062/DC1](https://advances.sciencemag.org/cgi/content/full/6/30/eaba1062/DC1))

Movie S1

**table S1.** Comparison of different mechanotransduction mechanisms (3, 12, 20, 37-38)

Sensing Mechanisms		Detectable Mechanical Stimulus	Power Consumption	Resistance to Strain Interference	Electrode Configuration of Sensor Array	Data Acquisition of Sensor Array
Active sensing mechanisms	<i>Resistive</i>	Static and slowly-varying stimulus	High	Poor	Dual-electrode	One-by-one operation
	<i>Capacitive</i>	Static and slowly-varying stimulus	Medium	–	Dual-electrode and crossed-grid electrode	One-by-one operation
	<i>Transistor-based</i>	Static and slowly-varying stimulus	High	Poor	Triple-electrode	One-by-one operation
Passive sensing mechanisms	<i>Piezoelectric</i>	Dynamic	Ultralow (Self-powered)	–	Dual-electrode	–
	<i>Triboelectric</i>	Dynamic	Ultralow (Self-powered)	–	Dual-electrode and single-electrode	–
	<i>Potentiometric ( This work )</i>	<b>Static and slowly-varying stimulus</b>	<b>Ultralow ( Self-powered )</b>	<b>Excellent ( Strain-insensitive )</b>	<b>Single-electrode ( Improved pixel density )</b>	<b>Simultaneous operation ( Enhanced data acquisition speed )</b>

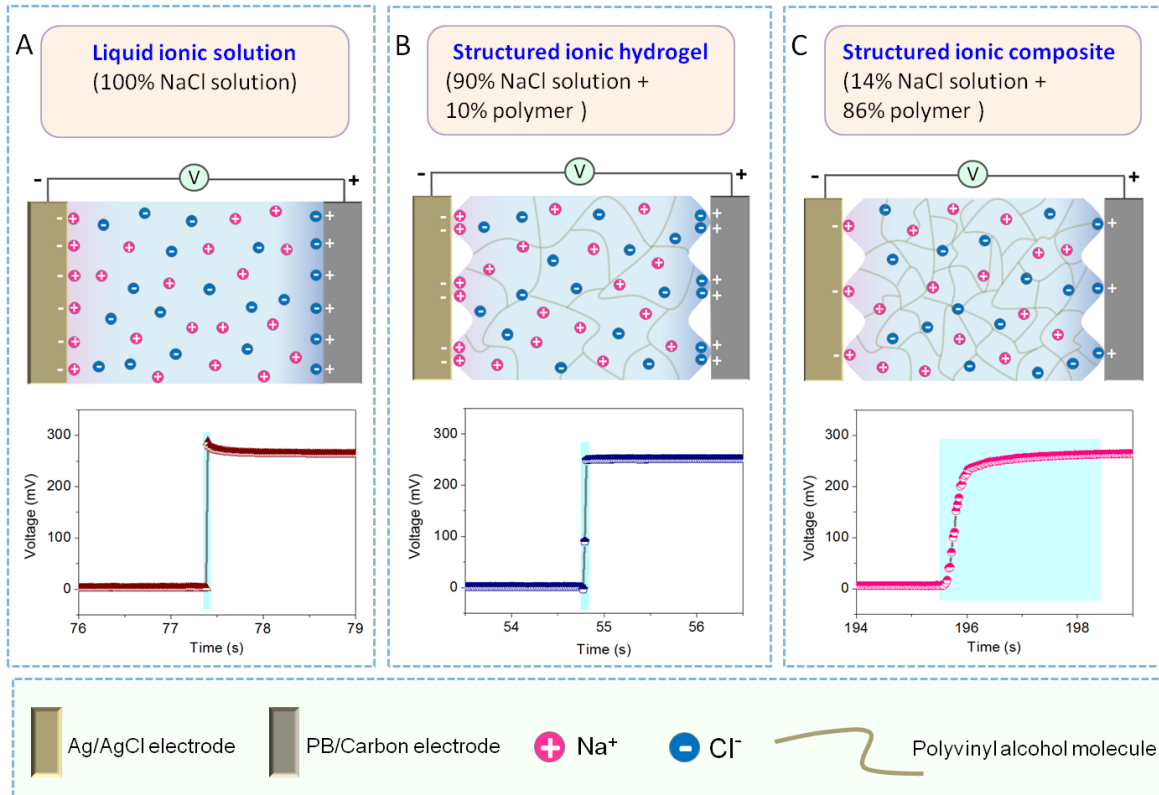


**fig. S1. Structural and component manipulation of the electrolyte for continuous and smooth mechanotransduction.** (A-C) Schematic illustrations showing the response behaviors of different potentiometric devices when bringing two electrodes (PB/carbon and Ag/AgCl) into contact with different types of electrolytes: (A) liquid ionic solution (100% NaCl solution), (B) microstructured ionic hydrogel ( $\approx 10\%$  polymer and  $\approx 90\%$  NaCl solution), and (C) microstructured ionic composite ( $\approx 84\%$  polymer and  $\approx 16\%$  NaCl solution).

As shown in fig. S1A-B, the development of potential difference between the two electrodes is too fast to manipulate when they are brought into contact with liquid NaCl solution and structured ionic hydrogel. This is because the ion mobility and electrical conductance of these electrolytes are very high. Even a small contact between the electrodes and electrolyte could lead to the full development of the potential difference. So, devices based on these electrolytes have only ‘OFF’ and ‘ON’ states and cannot be used to monitor mechanical stimuli in a continuous way.

To achieve a continuous mechanotransduction process, regulating the ion mobility and the electrical impedance of the electrolyte is needed. In fig. S2, we show that we can modulate the impedance of the electrolyte by tuning the water content. By this method, we can regulate the potential difference output between the electrodes. Therefore, we eventually employ ionic composites of relatively low water content and high electrical impedance as the electrolyte. We also create microstructure on the surface of the ionic composites, which enables to gradually regulate the electrode/electrolyte interface. As a result, a smooth upswing of the potential difference output is observed when bringing the electrodes into contact with the microstructured ionic composites, realizing a continuous and smooth potentiometric mechanotransduction process (fig. S1C).

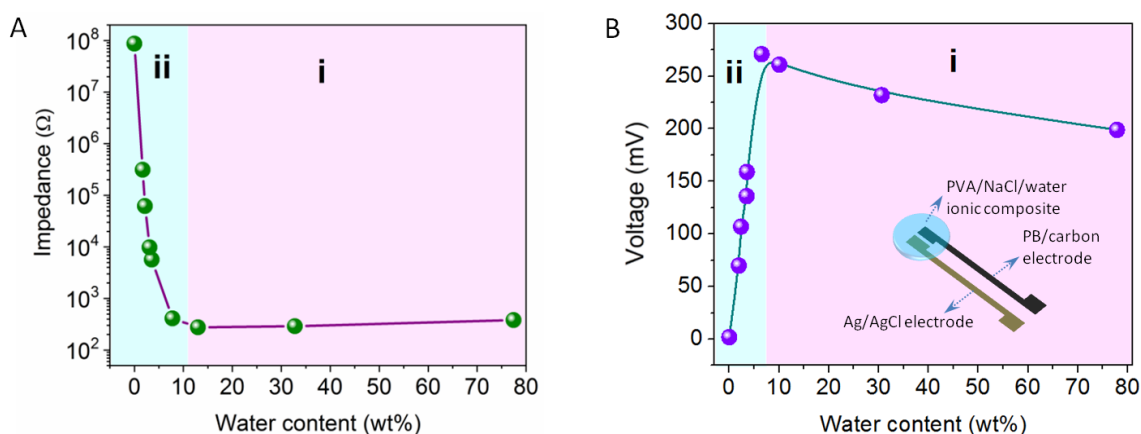


**fig. S2. Property regulation of PVA/NaCl/water electrolyte by tuning the water content.** The electrical impedance of the PVA/NaCl/water system is closely relevant to the relative water content. At high water content, the polymer chains are diluted by water molecules and the ions can move freely through the free volume between polymer chains, resulting in high ionic mobility and low electrical impedance (39-40). By contrast, reducing the water content could increase the density of polymer networks, which hinders the free movement of ions and increases the electrical impedance of this system. Here, we investigated the effect of relative water content on the electrical properties and electrochemical properties of the PVA/NaCl/water electrolyte. As shown in fig. S2A, the plot of electrical impedance (at 1 kHz) vs water content can be divided into two phases. In phase *i*, the impedance shows a slight decrease when reducing the water content because the ion concentration increases in this process. However, in phase *ii*, the impedance shows a prominent increase when further reducing the water content. This is because the highly-dense polymer network blocks the free movement of ions. The electrical property of the PVA/NaCl/water electrolyte has a great effect on its electrochemical behavior. As shown in fig. S2B, when bringing the electrolyte into contact with PB/carbon and Ag/AgCl electrodes, the measured potential difference output at different water contents shows a reverse trend with that of impedance change. This can be attributed to the internal impedance of the electrolyte, which restrains the potential difference output. For the proposed potentiometric mechanotransduction mechanism, an electrolyte with relatively high impedance is needed for effective and efficient regulation of the potential difference output between the electrodes, as discussed in fig. S1. Therefore, we eventually employ ionic composites with relatively low water content and high impedance as the electrolyte, which enables a gradual release of the potential difference between the electrodes when subjected to an external stimulus.

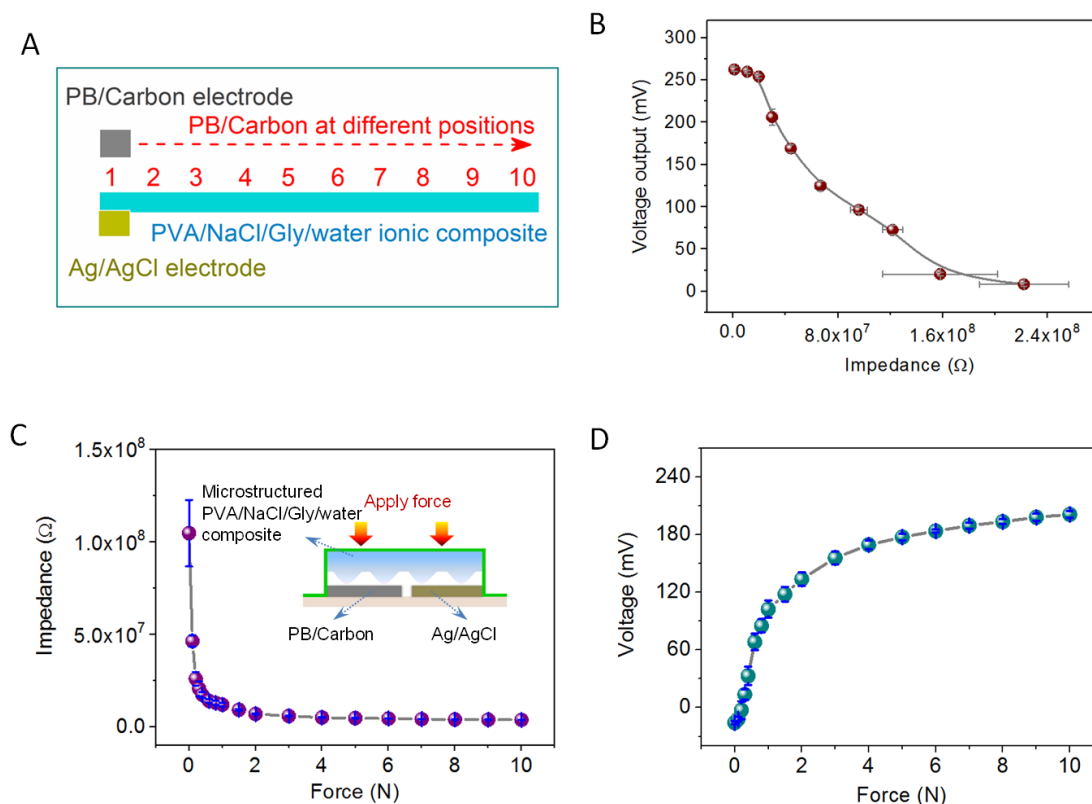


**fig. S3. Discussion on the working mechanism of the proposed potentiometric mechanotransduction.** (A-B) Schematic diagram along with the voltage output and the impedance measured between the two electrodes when fixing one electrode (Ag/AgCl) on one end of a strip-shaped PVA/NaCl/Gly/water ionic composite and moving the other electrode (PB/Carbon) to different positions along the strip-shaped ionic composite. (C-D) The measured impedance and voltage signal output between the two electrodes when applying different forces onto a mechanotransducer.

Based on the results presented in fig. S1, fig. S2, and fig. S3, the working mechanism of this potentiometric mechanotransduction process is fully discussed in the following. It is worth pointing out that regulating the water content of the electrolyte and creating microstructure on the electrolyte surface play a crucial role for the continuous and smooth mechanotransduction process, as demonstrated in fig. S1 and fig. S2. Thermodynamically, once the ion concentration of the electrolyte is fixed, the intrinsic potential difference between the two electrodes is also fixed. Thus, we can only change the output capability of the intrinsic potential difference via modulating the electrolyte/electrode interface. For the electrolytes based on NaCl solution and NaCl-containing hydrogel (fig.S1), their impedance is very low, which is measured at the magnitude of kilo-ohms. Such low impedance is not powerful enough to regulate the output capability of the intrinsic potential difference between the two electrodes, and the development of the potential difference between the two electrodes is too fast to manipulate, as demonstrated in fig.S1. Therefore, an electrolyte with reduced water content and relatively high impedance (as demonstrated in fig. S2) is needed to effectively regulate the potential difference output between the two electrodes.

To demonstrate the inference that we can regulate the potential difference output via modulating the internal impedance between the two electrodes, we designed a

straightforward experiment, as illustrated in fig. S3A. Specifically, we employed a strip-shaped PVA/NaCl/Gly/water ionic composite (the same composite as we used for fabricating our mechanotransducer) with high impedance as the electrolyte, and fixed the Ag/AgCl electrode on one end of this strip-shaped electrolyte. Then, we moved the other electrode (PB/Carbon electrode) to different positions along the strip-shaped electrolyte (fig. S3A), while measuring the impedance and the voltage output between the two electrodes. In this way, the material system, the device structure, and the ion concentration are all kept constant, and we are only changing the distance between the two electrodes and the internal impedance between the electrodes. As shown in fig. S3B, as we increased the distance between the two electrodes, the impedance between them increased significantly to hundreds of mega-ohms (measured by an LCR meter). At the same time, the recorded voltage output between the two electrodes decreased rapidly and eventually no voltage output was observed. This straightforward experiment provides solid evidence for the significant correlation between the internal impedance between the electrodes and the output capability of the voltage signal.

To further verify the mechanism proposed above, we measured the impedance and the voltage output of a mechanotransducer during applying different forces on it. As shown in fig. S3C, increasing the applied force can increase the contact area at the electrolyte/electrode interface, and thus can reduce the interfacial impedance significantly. At the same time, increasing the applied force results in a gradual release of the potential difference between the two electrodes, as demonstrated in fig. S3D. This synchronous variation of the measured impedance and the voltage output further demonstrate the close relationship between them.

For our proposed mechanotransducers, the successful and efficient regulation of the voltage output by externally applied force relies on two aspects: the high impedance ionic composite and the microstructure. We employed PVA/NaCl/Gly/water ionic composite with low water content and high impedance as the electrolyte, rather than NaCl solution or NaCl-containing hydrogel with low impedance as the electrolyte, as clearly demonstrated in fig. S1. In addition, we created uniform microstructure on the surface of the PVA/NaCl/Gly/water ionic composite, which further enables us to regulate the interfacial impedance effectively and efficiently. Benefiting from these two aspects, a continuous and smooth mechanotransduction process is demonstrated in this work.

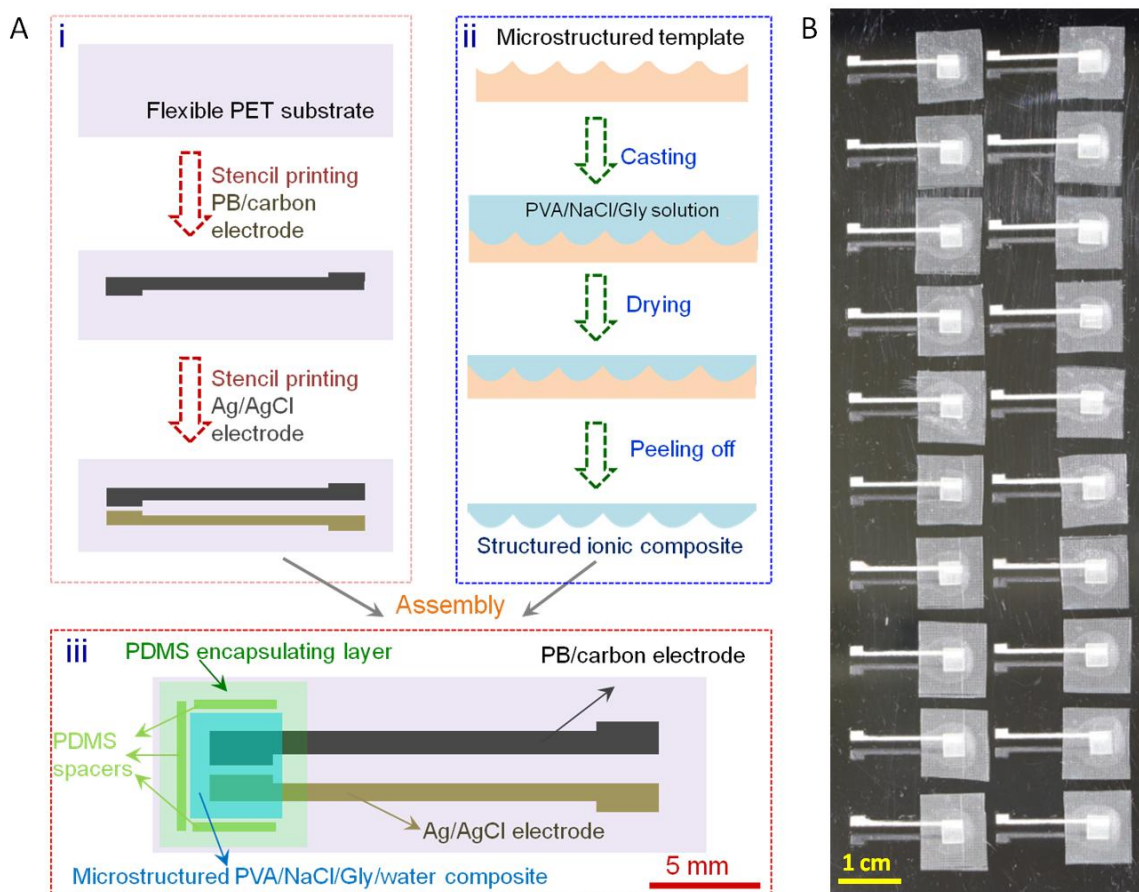


**fig. S4. All-solution processing fabrication of the potentiometric mechanotransducers.**

(A) Schematic diagram showing the all-solution processing fabrication of the potentiometric mechanotransducers using all commercially available materials. Three steps are involved: (i) stencil-printing PB/carbon and Ag/AgCl electrodes on a flexible substrate using commercial inks; (ii) solution casting PVA/NaCl/Gly solution onto a micro-patterned template to prepare the microstructured PVA/NaCl/Gly/water films; and (iii) final assembly of the potentiometric mechanotransducers. See *Experimental Section* for the details. (B) Photograph of an array of 20 potentiometric mechanotransducers fabricated in one batch, exhibiting good scalability and cost-efficiency. Photo Credit: Xiaodong Wu, University of California, Berkeley.

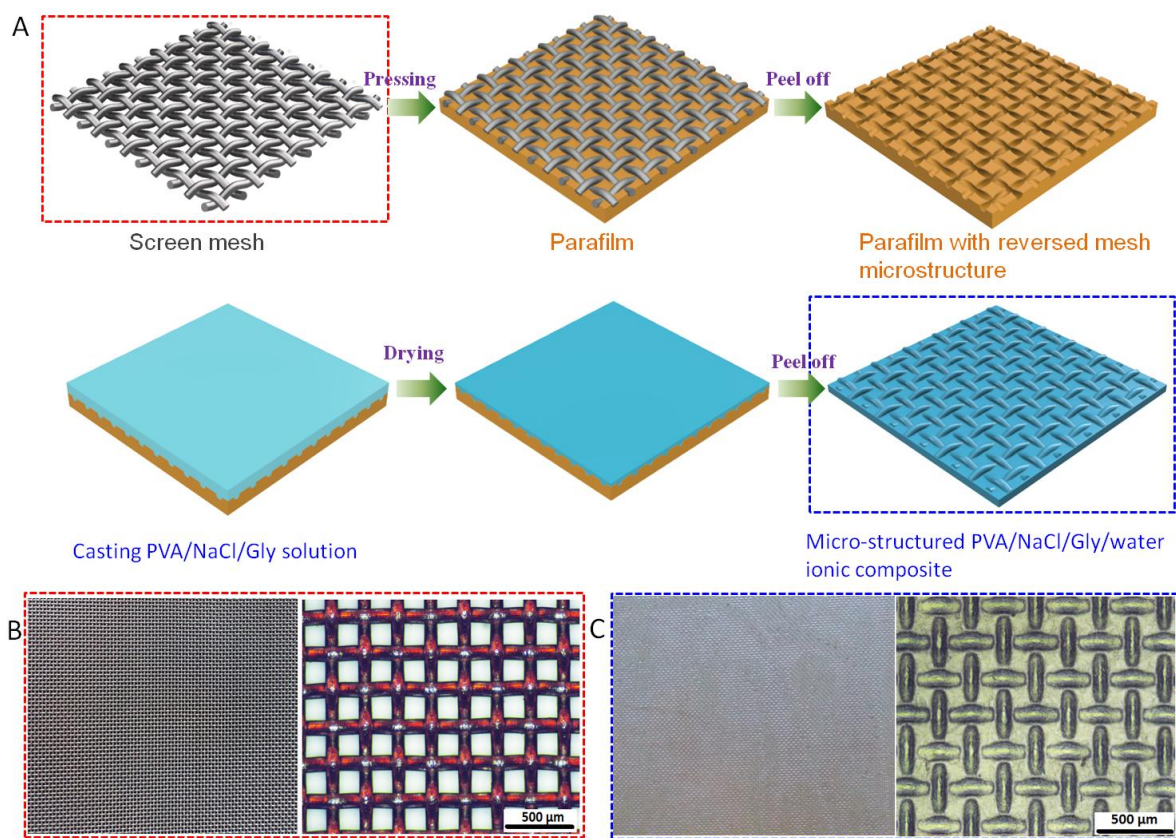


**fig. S5. Scalable fabrication of microstructured ionic composite via a mesh-molding strategy.** (A) Schematic diagram showing the fabrication flow of the microstructured PVA/NaCl/Gly/water ionic composite using a mesh-molding method. First, a pre-cleaned stainless-steel screen mesh (100 mesh count) is pressed into a ceraceous template (made by stacking 5 layers of Parafilm® on a glass plate) under about 1.0 MPa for 10 min at ambient temperature. Subsequently, the screen mesh embedded in the ceraceous template is placed into a freezer ( $\approx -20\text{ }^{\circ}\text{C}$ ) for 2 h, followed by quickly peeling off the screen mesh from the ceraceous template. A micro-patterned template with an inverse mesh structure is prepared. Then, PVA/NaCl/Gly aqueous solutions with desired components are cast onto the micro-patterned template. After drying the solution, microstructured PVA/NaCl/Gly/water ionic composite films are obtained. (B) Photograph and optical image of the screen mesh used as a template. (C) Photograph and optical image of the as-prepared microstructured PVA/NaCl/Gly/water ionic composite film. Scale bars of the optical images in B and C are 500  $\mu\text{m}$ . Photo Credit: Xiaodong Wu, University of California, Berkeley.



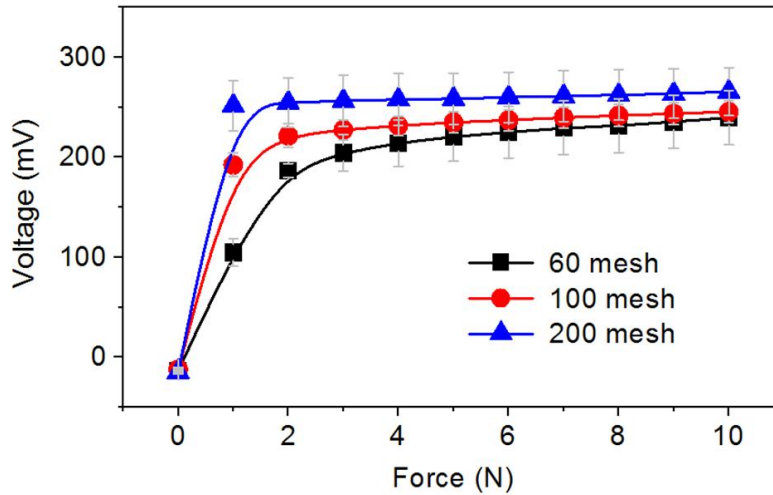
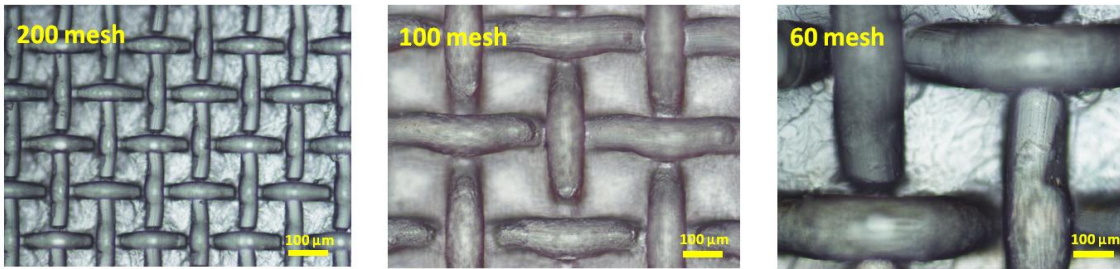


**fig. S6. Force sensing behaviors of mechanotransducers fabricated with ionic composites of different microstructure size.** Scale bars of the optical images are 100  $\mu\text{m}$ .

The influence of the microstructure size on the sensing behavior of the mechanotransducer is investigated. We used mesh-molded microstructures with 200, 100, and 60 mesh-sizes, respectively. From the plots of voltage output versus the applied force, we can see that mechanotransducer with smaller microstructure size shows higher sensitivity in low force range, while the signal variation gets saturated rapidly, which means that the detection range is narrow. In contrast, mechanotransducer with larger microstructure size shows lower sensitivity while exhibits a broader detection range. This is because smaller microstructure is easier to deform under the applied force and the microstructured ionic composite can get into full contact with the electrodes easily, resulting in a saturation of the voltage output. However, the larger microstructure is more resistant to force-induced deformation and enables to detect larger force.

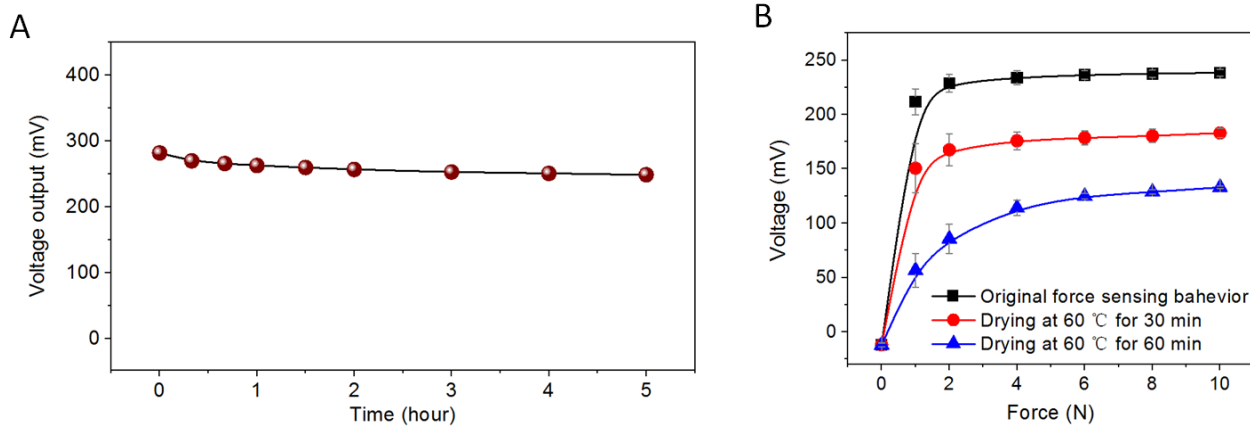


**fig. S7. Sensing behaviors of the mechanotransducers under harsh conditions. (A)** Continuous and long-term voltage output of a mechanotransducer. **(B)** Effect of baking a mechanotransducer at high temperature on its sensing behavior.

We tested the durability of the mechanotransducers for continuous and long-term operation. As shown in fig. S7A, after voltage output for 5 hours continuously, the signal exhibits a slight decline. During the long-term voltage output, the chemical reactions are happening continuously. Although the potentiometric measurement is claimed to have no current passing through the circuitry ideally, in practice, there is always a very small current, which can dissipate the internal electrochemical energy stored in the mechanotransducer very gradually. However, this proposed potentiometric sensor is a passive sensor. More specifically, most of the time, the sensor is under servo state (i.e. ‘OFF’ state). Only when an external stimulus is applied on the sensor, then the sensor can be activated and starts to output voltage signal. Once the external stimulus is released, the voltage output is cut off again. Because of this passive sensing mode, the operation time can be significantly extended.

As the mechanotransducers contain water in the electrolyte, component variation of the mechanotransducers should be considered for their practical use. To avoid electrolyte drying of the mechanotransducers, firstly, we employed Glycerol (Gly) as a humectant, which can binder with water molecules firmly and thus can lock the water into the PVA/NaCl/Gly/water ionic composites. Besides, since we have dried and stabilized the PVA/NaCl/Gly/water ionic composites in ambient condition for a long time, the PVA/NaCl/Gly/water ionic composites for sensor fabrication have reached a steady state. Moreover, we used a PDMS layer to encapsulate the mechanotransducers to further alleviate the component variation of the sensor system. Through these measures, drying of the mechanotransducers is greatly minimized and the performance should be stable under ambient condition. However, high temperature can break the steady state of the sensor system. As shown in fig. S7B, after setting the mechanotransducer into a drying oven (60 °C) for a period of time, its performance changed. Specifically, after drying at 60 °C, the voltage output decreased with longer drying time. This is due to that drying the mechanotransducer at such a high temperature can break the steady state of the sensor system and leads to excessive drying of the electrolyte, resulting in higher stiffness and higher internal impedance of the PVA/NaCl/Gly/water ionic composite. Therefore, the proposed mechanotransducers are suitable for the use at ambient condition, not for the use at high temperature.

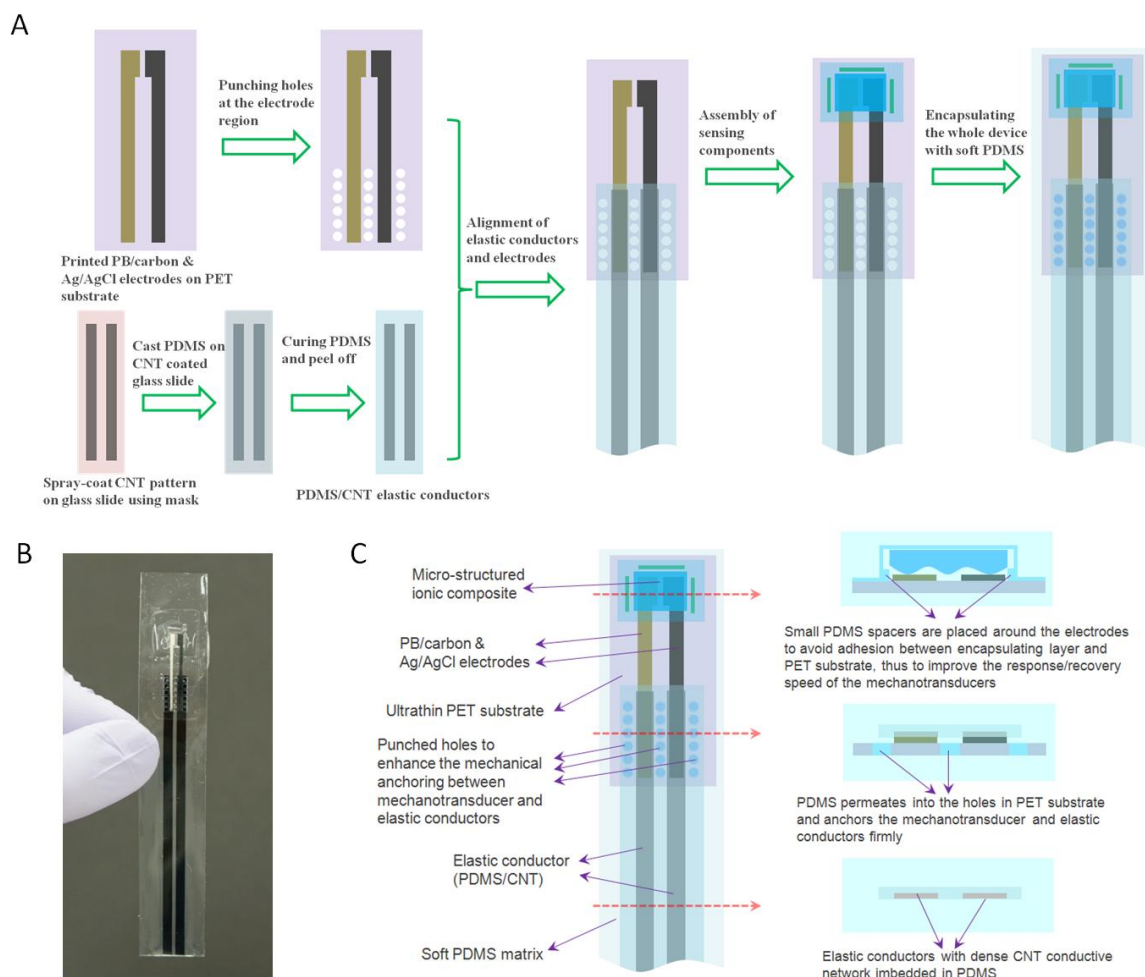


**fig. S8. Fabrication of stretchable mechanical sensors with strain-independent sensing performance.** (A) Schematic diagram showing the fabrication process flow of the stretchable sensors by combining the potentiometric mechanotransducers with elastic conductors. See *Experimental Section* for the fabrication details. Stretching deformation will cause variation in the resistance of the elastic conductors, while the sensor signal out can keep highly stable during the stretching process, exhibiting a strain-independent sensing behavior. (B) Photograph of a fabricated stretchable sensor. (C) Schematic illustrations showing the structural layout of the stretchable sensor. Photo Credit: Xiaodong Wu, University of California, Berkeley.

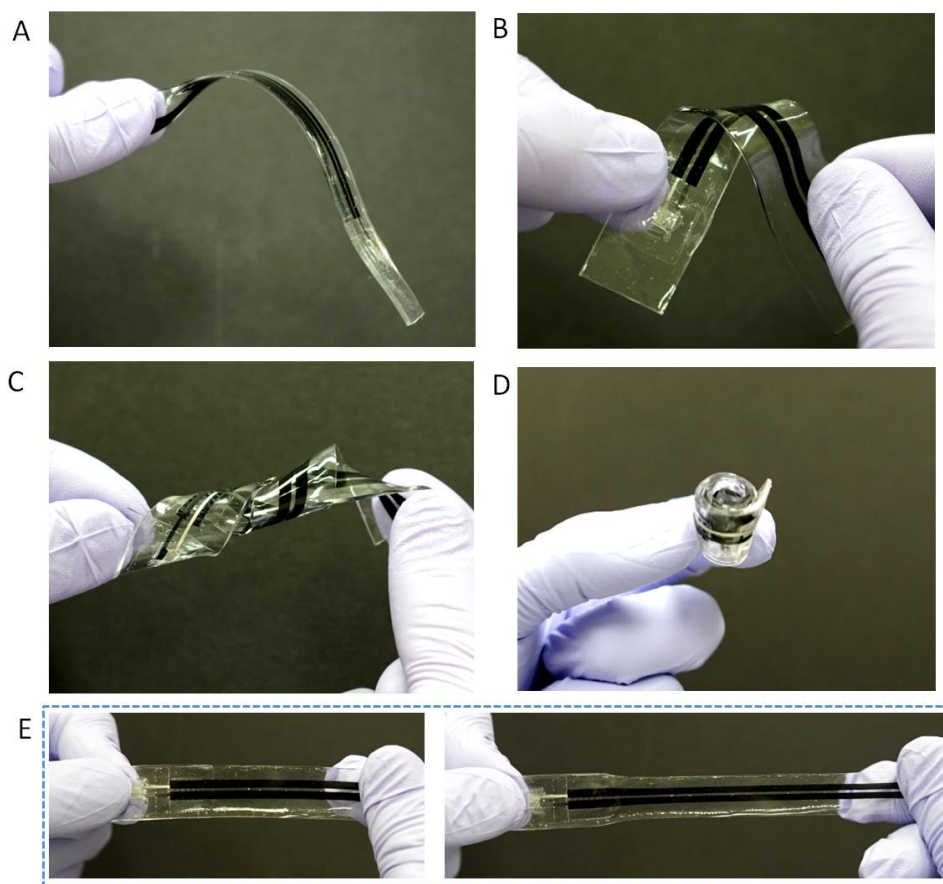


**fig. S9. Softness, flexibility, and stretchability of the strain-insensitive sensors.** Photographs showing a sensor that is (A) held at one end, (B) bent to  $180^\circ$ , (C) twisted to  $720^\circ$ , (D) rolled up, and (E) stretched to 50% strain, respectively, showing excellent softness, flexibility, and good stretchability of this sensor. Photo Credit: Xiaodong Wu, University of California, Berkeley.

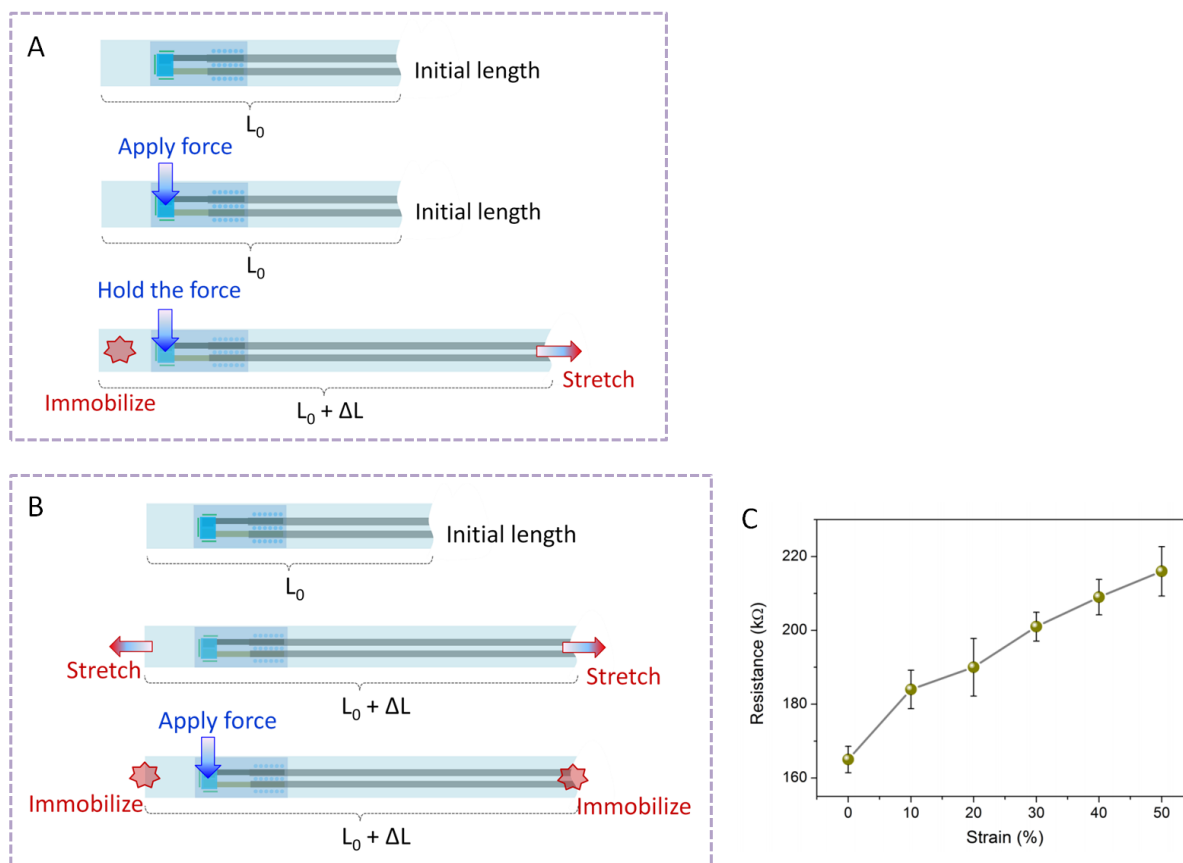
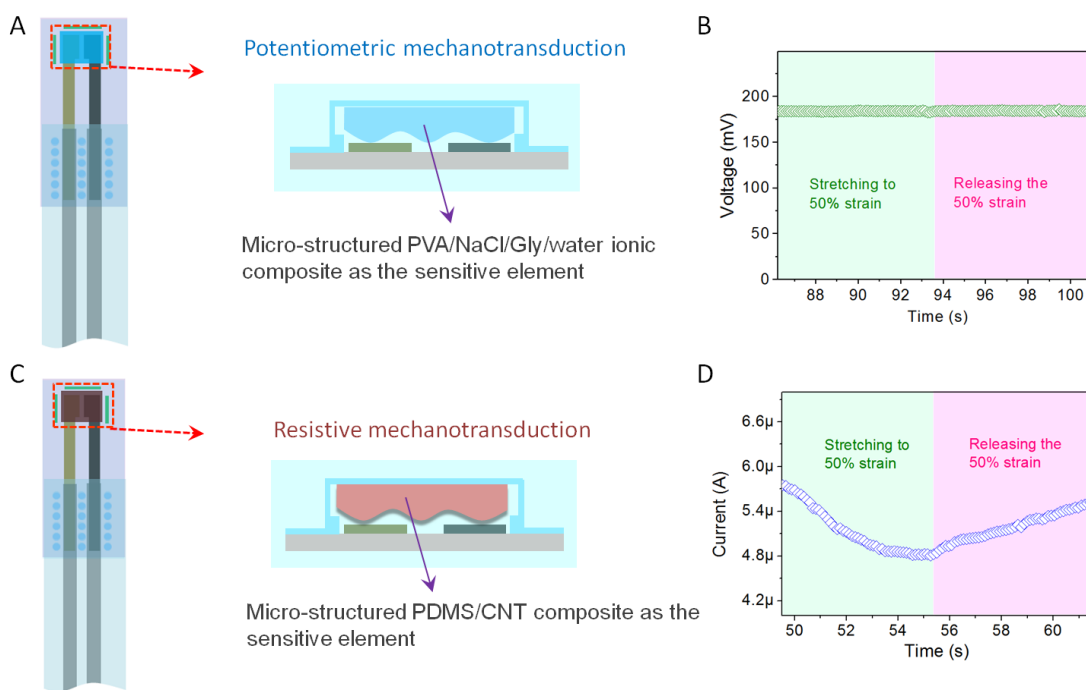


**fig. S10. Characterization of strain-insensitivity of the stretchable mechanical sensor.**

(A) Schematic diagram showing the characterization of strain-insensitivity by first applying a force on the sensor and then applying an increasing strain. (B) Schematic diagram showing the characterization of strain-insensitivity by first applying a strain on the sensor and then applying an increasing force. (C) Resistance change of the elastic conductors under the applied strain.

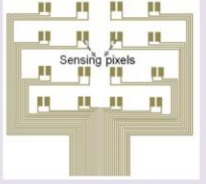
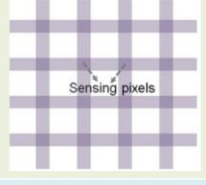
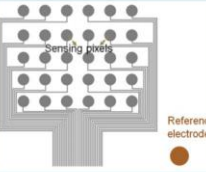
Since there are two critical factors (applied strain and applied force) during characterizing the strain-insensitive sensor and it is difficult to vary the applied force and the applied strain simultaneously, we need to fix one parameter and then vary the other one to evaluate the independence between these two factors. Firstly, by fixing the applied force and then changing the strain, we investigated the stretching interference to the stability of the sensor signal output (fig. S10A). We first applied a stable force onto the sensor to generate sensor signal output. Then, we stretched the sensor to different strains to see the strain-interference to the sensor signal output. As shown in Fig. 4D, the voltage output of the sensor keeps highly stable during the stretching process.

Secondly, by fixing the applied strain and then changing the force, we investigated the force response behaviors of the sensor under different strains (fig. S10B). We first pre-applied a strain onto the sensor (pre-stretched the sensor). Then, we applied different forces onto the active area of the pre-stretched sensor and measured the sensor's voltage output. As shown in Fig. 4F and Fig. 4G, The measured signals of the prestretched and unstretched sensors are nearly identical, indicating a good strain-independent sensing capability of the sensor.



**fig. S11. Stretching interference to the sensor performance based on different sensing mechanisms.** Here, we compare the sensing performance of potentiometric stretchable sensors and resistive stretchable sensors when they are subjected to stretching deformation (50% strain). To normalize the comparison, we only change the sensing elements at the sensing region (as the red dashed rectangle indicates) and keep all other components the same (including electrodes, substrates, geometry, size, etc). We use side-by-side PB/carbon electrode and Ag/AgCl electrode for both of the stretchable sensors. For the potentiometric sensors, we put a piece of microstructured PVA/NaCl/Gly/water ionic composite at the sensing region (**A**). In contrast, for the resistive sensors, we put a piece of microstructured conductive PDMS/CNT composite at the sensing region (**C**). To evaluate the sensors' behaviors under stretching deformation, firstly, a constant force is loaded on the sensors to generate sensor signals. Then, the sensors are gradually stretched to 50% strain, followed by releasing the strain. The sensor signals are monitored during the stretching/releasing process. Notably, the signal output of the potentiometric sensors is highly stable (less than 1% signal variation) during the stretching/releasing process, showing a strain-independent sensing performance (**B**). However, for the resistive sensors, the signal output shows a prominent drifting ( $\approx 21.3\%$  relative signal variation) during the stretching/releasing process due to the stretching interference (**D**). These results demonstrate the significant advantage of the potentiometric mechanotransduction mechanism for constructing stretchable sensors with strain-independent sensing performance, which is highly desired for stretchable electronics and systems.

**table S2.** Comparison of e-skins based on different electrode configurations

E-skin with $N$ sensing pixels	Layout	Pixel density	Operation and data acquisition speed	Power consumption
Dual-electrode		<ul style="list-style-type: none"> <li>- Low</li> <li>- Limited by the arrangement of massive connection wires (<math>2N</math>)</li> </ul>	<ul style="list-style-type: none"> <li>- High</li> <li>- Sensing pixels can be operated individually and possibly simultaneously</li> </ul>	<ul style="list-style-type: none"> <li>- High</li> <li>- Each sensing pixel consumes power to operate</li> </ul>
Crossed-grid		<ul style="list-style-type: none"> <li>- High</li> <li>- Only needs <math>2\sqrt{N}</math> connection wires</li> </ul>	<ul style="list-style-type: none"> <li>- Low</li> <li>- Sensing pixels need to be operated one-by-one to avoid cross-talk</li> </ul>	<ul style="list-style-type: none"> <li>- High</li> <li>- Each sensing pixel consumes power and there is also current leakage</li> </ul>
Single-electrode		<ul style="list-style-type: none"> <li>- Medium</li> <li>- Needs <math>N+1</math> connection wires</li> </ul>	<ul style="list-style-type: none"> <li>- High</li> <li>- Sensing pixels can be operated simultaneously</li> </ul>	<ul style="list-style-type: none"> <li>- Ultralow</li> <li>- Self-generated signal output</li> <li>- Less than 1 nW to operate a sensing pixel</li> </ul>

For the dual-electrode-mode e-skins, there need to be two connection wires for each pixel to acquire and transfer data. So, for an e-skin with  $N$  sensing pixels, there need to be  $2N$  connection wires. In contrast, for our single-electrode-mode e-skin, there only need to be  $N+1$  connection wires. Theoretically, for an e-skin with a large number of sensing pixels,  $N+1$  is far less than  $2N$ , which could simplify the fabrication and the arrangement of connection wires, allowing fabricating e-skin with relatively higher pixel density. Nevertheless, the crossed-grid e-skins need  $2\sqrt{N}$  connections, which is less than that of the single-electrode-mode e-skin ( $N+1$  connections) and easier to fabricate. So, the single-electrode-mode e-skin exhibits higher theoretical pixel density than that of the dual-electrode-mode e-skins, but the pixel density is lower than that of crossed-grid electrode mode e-skins. However, this single-electrode-mode e-skin has higher data acquisition speed than that of the crossed-grid electrode mode e-skins.

Overall, this single-electrode-mode e-skin achieves a good balance between pixel density and data acquisition speed. Furthermore, this single-electrode-mode e-skin shows a significant advantage over the other two electrode configurations regarding power consumption (less than 1 nW), which makes it very appealing and competitive for practical applications.

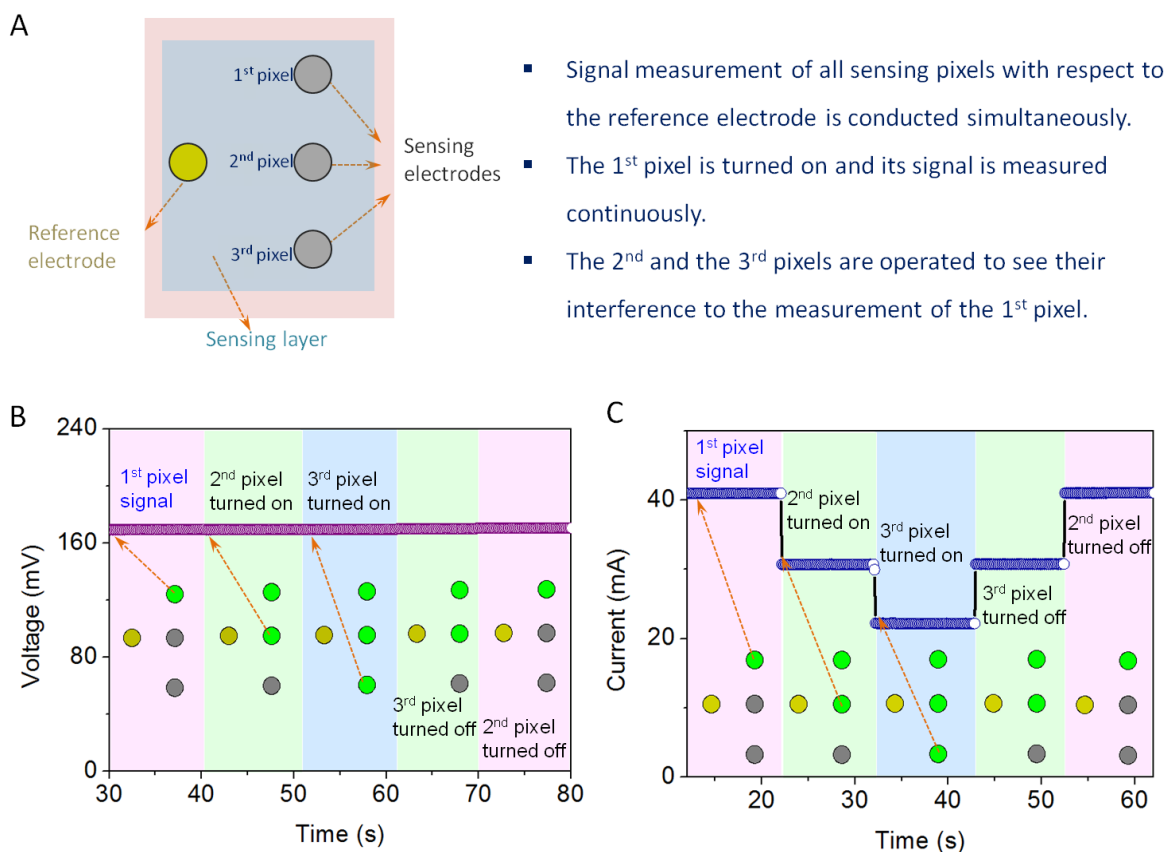


**fig. S12. Simultaneous data acquisition from all sensing pixels of single-electrode-mode e-skins based on potentiometric and resistive sensing mechanisms. (A)**

Schematic showing a simplified e-skin model with one reference electrode, three sensing electrodes, and a sensing layer placed on top of the electrodes. The signals of all sensing electrodes are measured simultaneously (using three sets of equipments) with respect to the reference electrode. At the resting state, all sensing pixels are off without signal output. By applying an external force on the sensing pixels, the sensing pixels are turned on, with signal output generated. To evaluate the interference between the sensing pixels during simultaneous operation, firstly, the 1<sup>st</sup> sensing pixel is turned on and its signal is measured continuously. Then, the 2<sup>nd</sup> and the 3<sup>rd</sup> sensing pixels are operated (turning on or turning off) to see their interference to the signal measurement of the 1<sup>st</sup> sensing pixel. For the potentiometric single-electrode-mode e-skin (**B**), we can see that the operation of the 2<sup>nd</sup> and the 3<sup>rd</sup> sensing pixels has a negligible effect on the measurement of the 1<sup>st</sup> sensing pixel. This is because there is nearly no current flow involved in the potentiometric measurement, so the interference and crosstalk between different pixels can be minimized or eliminated. However, for the resistive single-electrode-mode e-skin (**C**), operation of the 2<sup>nd</sup> and the 3<sup>rd</sup> sensing pixels causes a significant impact on the measurement of the 1<sup>st</sup> sensing pixel due to the interference and crosstalk between different sensing pixels. These results demonstrate the superiority of the potentiometric single-electrode-mode e-skin for simultaneous data acquisition from all sensing pixels, which can greatly enhance the data acquisition speed of future e-skins.



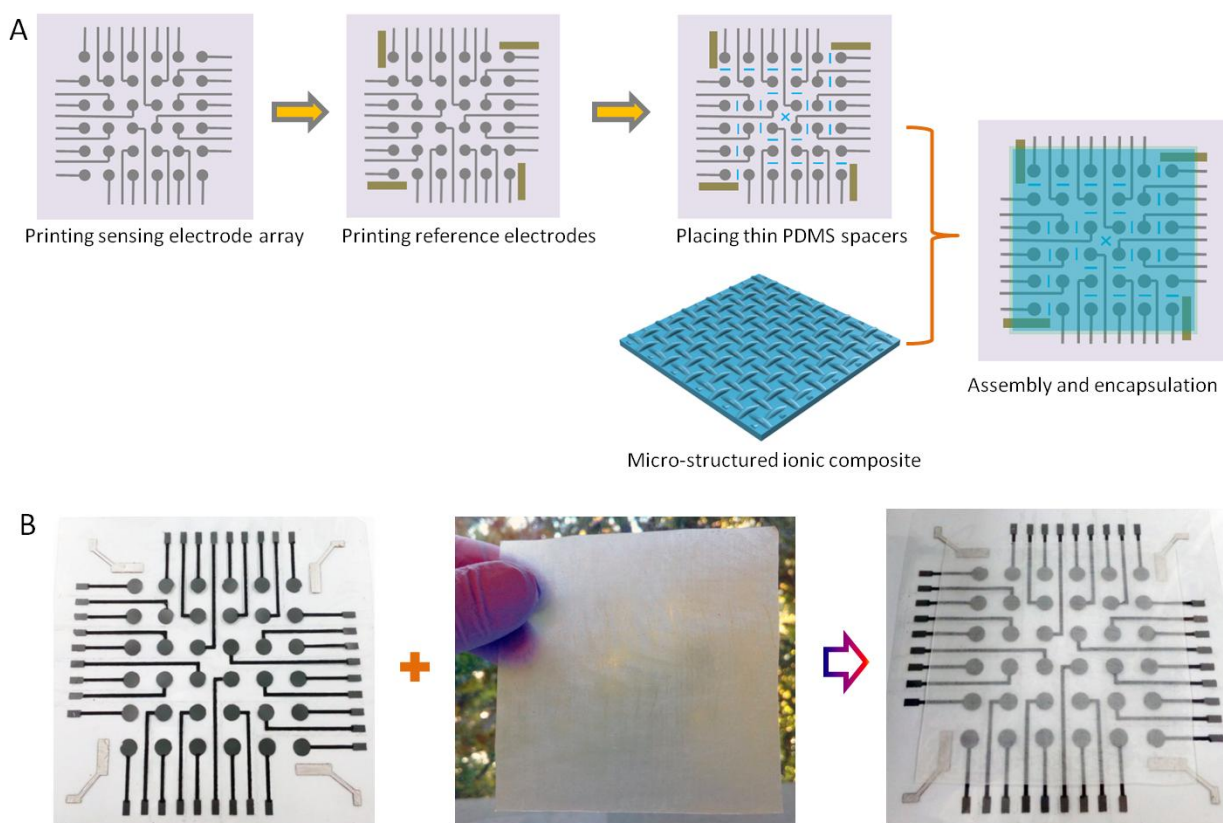


**fig. S13. Fabrication of the single-electrode-mode e-skin.** (A) Schematic diagram illustrating the construction process of the single-electrode-mode e-skin. First, PB/carbon and Ag/AgCl electrodes are printed on a flexible substrate. Then, thin PDMS spacers are placed on the pre-defined positions, followed by pasting PVA/NaCl/Gly glue on the Ag/AgCl electrodes. Finally, a microstructured PVA/NaCl/Gly/water ionic composite film is put on the electrodes and the whole e-skin is encapsulated using a thin PDMS layer. (B) Photographs showing the assembly of the single-electrode-mode e-skin using printed electrode pattern and microstructured PVA/NaCl/Gly/water ionic composite film. Photo Credit: Xiaodong Wu, University of California, Berkeley.

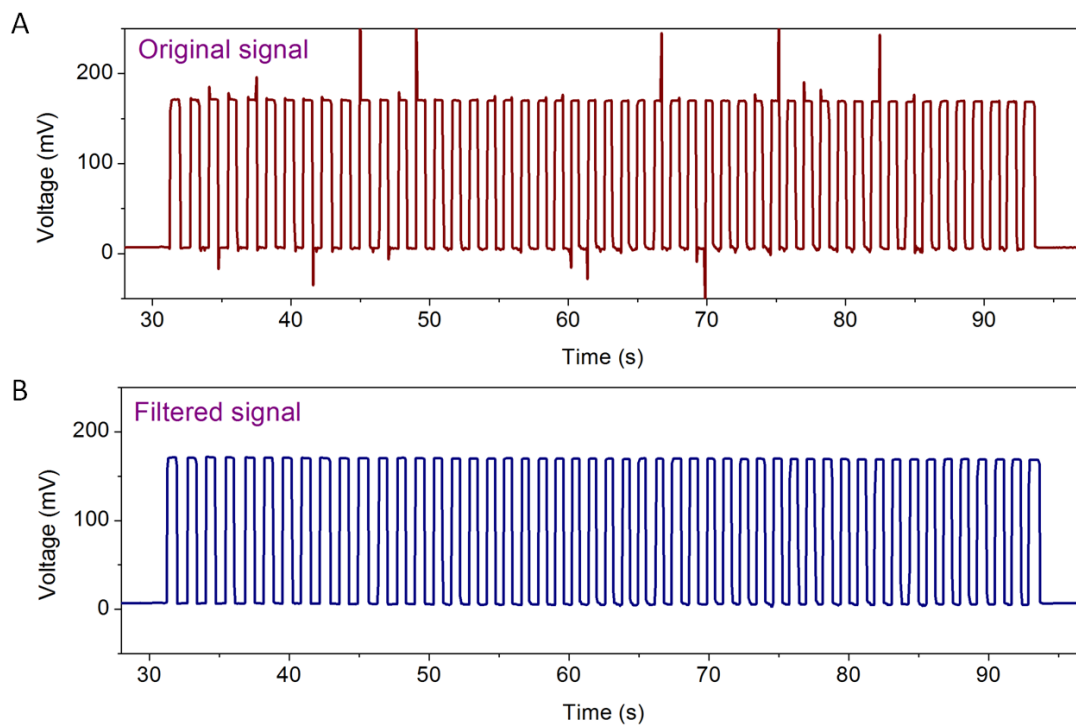


**fig. S14. Minimizing triboelectric interference via signal processing.** (A) Recorded pristine signal output of a potentiometric mechanotransducer. Some spike peaks appear occasionally as a result of the triboelectric effect, which could cause interference to the sensor signals. Nevertheless, these triboelectric spikes are very sharp and can be easily filtered by subsequent signal processing. (B) Processed signal with the triboelectric spikes filtered. Such signal processing enables us to minimize the triboelectric interference to the potentiometric mechanotransduction process.

## REFERENCES AND NOTES

1. H.-H. Chou, A. Nguyen, A. Chortos, J. W. F. To, C. Lu, J. Mei, T. Kurosawa, W.-G. Bae, J. B.-H. Tok, Z. Bao. A chameleon-inspired stretchable electronic skin with interactive colour changing controlled by tactile sensing. *Nat. Commun.* **6**, 8011 (2015).
2. Y. Wu, Y. Liu, Y. Zhou, Q. Man, C. Hu, W. Asghar, F. Li, Z. Yu, J. Shang, G. Liu, M. Liao, R.-W. Li. A skin-inspired tactile sensor for smart prosthetics. *Sci. Robot.* **3**, eaat0429 (2018).
3. A. Chortos, J. Liu, Z. Bao. Pursuing prosthetic electronic skin. *Nat. Mater.* **15**, 937–950 (2016).
4. X. Wang, L. Dong, H. Zhang, R. Yu, C. Pan, Z. L. Wang. Recent progress in electronic skin. *Adv. Sci.* **2**, 1500169 (2015).
5. Z. Wang, S. Guo, H. Li, B. Wang, Y. Sun, Z. Xu, X. Chen, K. Wu, X. Zhang, F. Xing, L. Li, W. Hu. The semiconductor/conductor interface piezoresistive effect in an organic transistor for highly sensitive pressure sensors. *Adv. Mater.* **31**, e1805630 (2018).
6. Y. Zang, F. Zhang, D. Huang, X. Gao, C.-a. Di, D. Zhu. Flexible suspended gate organic thin-film transistors for ultra-sensitive pressure detection. *Nat. Commun.* **6**, 6269 (2015).
7. C. M. Boutry, Y. Kaizawa, B. C. Schroeder, A. Chortos, A. Legrand, Z. Wang, J. Chang, P. Fox, Z. Bao. A stretchable and biodegradable strain and pressure sensor for orthopaedic application. *Nat. Electron.* **1**, 314–321 (2018).
8. Z. Zou, C. Zhu, Y. Li, X. Lei, W. Zhang, J. Xiao. Rehealable, fully recyclable, and malleable electronic skin enabled by dynamic covalent thermoset nanocomposite. *Sci. Adv.* **4**, eaaq0508 (2018).
9. Y. Cao, Y. J. Tan, S. Li, W. W. Lee, H. Guo, Y. Cai, C. Wang, B. C.-K. Tee. Self-healing electronic skins for aquatic environments. *Nat. Electron.* **2**, 75–82 (2019).
10. S. Wang, J. Xu, W. Wang, G.-J. N. Wang, R. Rastak, F. Molina-Lopez, J. W. Chung, S. Niu, V. R. Feig, J. Lopez, T. Lei, S.-K. Kwon, Y. Kim, A. M. Foudeh, A. Ehrlich, A. Gasperini, Y. Yun, B.

- Murmann, J. B.-H. Tok, Z. Bao. Skin electronics from scalable fabrication of an intrinsically stretchable transistor array. *Nature* **555**, 83–88 (2018).
11. J. Xu, S. Wang, G.-J. N. Wang, C. Zhu, S. Luo, L. Jin, X. Gu, S. Chen, V. R. Feig, J. W. F. To, S. Rondeau-Gagné, J. Park, B. C. Schroeder, C. Lu, J. Y. Oh, Y. Wang, Y.-H. Kim, H. Yan, R. Sinclair, D. Zhou, G. Xue, B. Murmann, C. Linder, W. Cai, J. B.-H. Tok, J. W. Chung, Z. Bao. Highly stretchable polymer semiconductor films through the nanoconfinement effect. *Science* **355**, 59–64 (2017).
  12. K.-Y. Chun, Y. J. Son, E.-S. Jeon, S. Lee, C.-S. Han. A self-powered sensor mimicking slow- and fast-adapting cutaneous mechanoreceptors. *Adv. Mater.* **30**, e1706299 (2018).
  13. G. S. Cañón Bermúdez, D. D. Karnaushenko, D. Karnaushenko, A. Lebanov, L. Bischoff, M. Kaltenbrunner, J. Fassbender, O. G. Schmidt, D. Makarov. Magnetosensitive e-skins with directional perception for augmented reality. *Sci. Adv.* **4**, eaao2623 (2018).
  14. G. S. Cañón Bermúdez, H. Fuchs, L. Bischoff, J. Fassbender, D. Makarov. Electronic-skin compasses for geomagnetic field-driven artificial magnetoreception and interactive electronics. *Nat. Electron.* **1**, 589–595 (2018)
  15. C.-C. Kim, H.-H. Lee, K. H. Oh, J.-Y. Sun. Highly stretchable, transparent ionic touch panel. *Science* **353**, 682–687 (2016).
  16. N. Sperlakis, *Cell Physiology Source Book* (Academic Press, ed. 4, 2012). chap. 36, pp. 633–647.
  17. R. Ikeda, M. Cha, J. Ling, Z. Jia, D. Coyle, J. G. Gu, Merkel cells transduce and encode tactile stimuli to drive A $\beta$ -afferent impulses. *Cell* **157**, 664–675 (2014).
  18. M. L. Jin, S. Park, Y. Lee, J. H. Lee, J. Chung, J. S. Kim, J.-S. Kim, S. Y. Kim, E. Jee, D. W. Kim, J. W. Chung, S. G. Lee, D. Choi, H.-T. Jung, D. H. Kim. An ultrasensitive, visco-poroelastic artificial mechanotransducer skin inspired by piezo2 protein in mammalian merkel cells. *Adv. Mater.* **29**, 1605973 (2017).

19. C. Hammond, *Cellular and Molecular Neurophysiology* (Academic Press, ed. 4, 2015). chap. 3, pp. 39–54.
20. J. Park, Y. Lee, M. Ha, S. Cho, H. Ko. Micro/nanostructured surfaces for self-powered and multifunctional electronic skins. *J. Mater. Chem. B* **4**, 2999–3018 (2016).
21. X. Xie, M. Ye, C. Liu, P.-C. Hsu, C. S. Criddle, Y. Cui. Use of low cost and easily regenerated Prussian Blue cathodes for efficient electrical energy recovery in a microbial battery. *Energ. Environ. Sci.* **8**, 546–551 (2015).
22. Z. L. Wang, J. Chen, L. Lin. Progress in triboelectric nanogenerators as a new energy technology and self-powered sensors. *Energ. Environ. Sci.* **8**, 2250–2282 (2015).
23. J. K. Moon, J. Jeong, D. Lee, H. K. Pak. Electrical power generation by mechanically modulating electrical double layers. *Nat. Commun.* **4**, 1487 (2013).
24. J. Zhao, S. Han, Y. Yang, R. Fu, Y. Ming, C. Lu, H. Liu, H. Gu, W. Chen. Passive and space-discriminative ionic sensors based on durable nanocomposite electrodes toward sign language recognition. *ACS Nano* **11**, 8590–8599 (2017).
25. F. H. J. van der Heyden, D. J. Bonthuis, D. Stein, C. Meyer, C. Dekker. Power generation by pressure-driven transport of ions in nanofluidic channels. *Nano Lett.* **7**, 1022–1025 (2007).
26. Z. Huang, Y. Hao, Y. Li, H. Hu, C. Wang, A. Nomoto, T. Pan, Y. Gu, Y. Chen, T. Zhang, W. Li, Y. Lei, N. Kim, C. Wang, L. Zhang, J. W. Ward, A. Maralani, X. Li, M. F. Durstock, A. Pisano, Y. Lin, S. Xu, Three-dimensional integrated stretchable electronics. *Nat. Electron.* **1**, 473–480 (2018).
27. K. Sim, Z. Rao, H.-J. Kim, A. Thukral, H. Shim, C. Yu. Fully rubbery integrated electronics from high effective mobility intrinsically stretchable semiconductors. *Sci. Adv.* **5**, eaav5749 (2019).
28. C. Dagdeviren, Y. Shi, P. Joe, R. Ghaffari, G. Balooch, K. Usgaonkar, O. Gur, P. L. Tran, J. R. Crosby, M. Meyer, Y. Su, R. Chad Webb, A. S. Tedesco, M. J. Slepian, Y. Huang, J. A. Rogers, Conformal piezoelectric systems for clinical and experimental characterization of soft tissue biomechanics. *Nat. Mater.* **14**, 728–736 (2015).

29. S. Xu, Z. Yan, K.-I. Jang, W. Huang, H. Fu, J. Kim, Z. Wei, M. Flavin, J. McCracken, R. Wang, A. Badea, Y. Liu, D. Xiao, G. Zhou, J. Lee, H. U. Chung, H. Cheng, W. Ren, A. Banks, X. Li, U. Paik, R. G. Nuzzo, Y. Huang, Y. Zhang, J. A. Rogers, Assembly of micro/nanomaterials into complex, three-dimensional architectures by compressive buckling. *Science* **347**, 154–159 (2015).
30. S. Xu, Y. Zhang, J. Cho, J. Lee, X. Huang, L. Jia, J. A. Fan, Y. Su, J. Su, H. Zhang, H. Cheng, B. Lu, C. Yu, C. Chuang, T.-I. Kim, T. Song, K. Shigeta, S. Kang, C. Dagdeviren, I. Petrov, P. V. Braun, Y. Huang, U. Paik, J. A. Rogers, Stretchable batteries with self-similar serpentine interconnects and integrated wireless recharging systems. *Nat. Commun.* **4**, 1543 (2013).
31. A. Lamoureux, K. Lee, M. Shlian, S. R. Forrest, M. Shtein, Dynamic kirigami structures for integrated solar tracking. *Nat. Commun.* **6**, 8092 (2015).
32. T. C. Shyu, P. F. Damasceno, P. M. Dodd, A. Lamoureux, L. Xu, M. Shlian, M. Shtein, S. C. Glotzer, N. A. Kotov, A kirigami approach to engineering elasticity in nanocomposites through patterned defects. *Nat. Mater.* **14**, 785–789 (2015).
33. Q. Hua, J. Sun, H. Liu, R. Bao, R. Yu, J. Zhai, C. Pan, Z. L. Wang. Skin-inspired highly stretchable and conformable matrix networks for multifunctional sensing. *Nat. Commun.* **9**, 244 (2018).
34. D. J. Lipomi, M. Vosgueritchian, B. C.-K. Tee, S. L. Hellstrom, J. A. Lee, C. H. Fox, Z. Bao. Skin-like pressure and strain sensors based on transparent elastic films of carbon nanotubes. *Nat. Nanotechnol.* **6**, 788–792 (2011).
35. C. M. Boutry, M. Negre, M. Jorda, O. Vardoulis, A. Chortos, O. Khatib, Z. Bao. A hierarchically patterned, bioinspired e-skin able to detect the direction of applied pressure for robotics. *Sci. Robot.* **3**, eaau6914 (2018).
36. M. S. Sarwar, Y. Dobashi, C. Preston, J. K. M. Wyss, S. Mirabbasi, J. D. W. Madden. Bend, stretch, and touch: Locating a finger on an actively deformed transparent sensor array. *Sci. Adv.* **3**, e1602200 (2017).
37. Y. Zang, F. Zhang, C. Di, D. Zhu. Advances of flexible pressure sensors toward artificial intelligence and health care applications. *Mater. Horiz.* **2**, 140–156 (2015).

38. J. Li, R. Bao, J. Tao, Y. Peng, C. Pan. Recent progress in flexible pressure sensor arrays: From design to applications. *J. Mater. Chem. C* **6**, 11878–11892 (2018).
39. J. Wu, Z. Wu, H. Xu, Q. Wu, C. Liu, B.-R. Yang, X. Gui, X. Xie, K. Tao, Y. Shen, J. Miaod, L. K. Norforde. An intrinsically stretchable humidity sensor based on anti-drying, self-healing and transparent organohydrogels. *Mater. Horiz.* **6**, 595–603 (2019).
40. H. Ota, K. Chen, Y. Lin, D. Kiriya, H. Shiraki, Z. Yu, T.-J. Ha, A. Javey. Highly deformable liquid-state heterojunction sensors. *Nat. Commun.* **5**, 5032 (2014).